

DOI: 10.1002/ ((please add manuscript number))

Article type: Full Paper

Title

Single-step preparation of large area TiO₂ photoelectrodes for water splitting

*Silvia Franz**, *Hamed Arab*, *Gian Luca Chiarello*, *Massimiliano Bestetti*, and *Elena Selli*

E-mail: silvia.franz@polimi.it

Keywords: TiO₂, thin films, plasma electrolytic oxidation, photocatalytic water splitting, photoelectrochemical cell

Abstract

The fast, single-step and easily scalable production by Plasma Electrolytic Oxidation (PEO) of large area TiO₂ electrodes with excellent photoactivity in water splitting under simulated solar light is here investigated systematically. In particular, the effects that the cell voltage (100-180 V) and the processing time (0.5-15 min) have on the electrode properties have been studied. The PEO-produced oxide layers are porous, the predominant crystalline structure shifting from anatase, to an anatase-rutile mixture, and finally to rutile by rising the cell voltage. The electrodes show a double-layered structure, with a more compact layer at the interface with the titanium substrate and a thick porous layer on the external surface. The photocurrent density *vs.* wavelength reflects the phase composition, with a maximum incident photon to current efficiency of 90% at 320 nm. The highest H₂ production rate was attained with the mixed anatase-rutile electrode prepared by 300 s-long PEO at 150 V.

1. Introduction

Titanium dioxide is a wide band gap semiconductor naturally occurring in three allotropic phases anatase, rutile and brookite. Owing to its nontoxicity, low cost, good chemical stability, and band energy levels suitable for excitation under UV-Vis irradiation, titanium dioxide and its doped variants are considered among the most viable electrode materials for photocatalytic

applications, such as water and air depollution, water splitting and CO₂ reduction ^[1-8]. Out of all techniques for the growth of thin films for photoelectrodes preparation ^[9-11], Plasma Electrolytic Oxidation allows to easily synthesise photoactive TiO₂ layers with tuned crystalline phase composition ^[12-14] and dosage of doping elements ^[15-21].

Plasma electrolytic oxidation (PEO), also referred to as micro-arc oxidation or micro-plasma oxidation or spark anodization, is a plasma-assisted conversion of a metal surface into a ceramic film. PEO is performed at operating potentials exceeding the breakdown voltage of the growing oxide so that electrical discharges develop at a number of separate sites of the oxide layer, locally inducing temperature and pressure values up to 10000 K and 10¹¹ Pa, respectively. The dielectric phase undergoes melting and both the gas and dielectric phases can be ionised, the electrode/electrolyte interface becoming a complex multiphase-phase system (dielectric-gas-plasma-electrolyte) with a number of different phase boundaries. Therefore, in addition to the electrode processes typical of electrochemical anodization (i.e. metal anodic dissolution, oxide formation and oxygen evolution), plasma thermochemical reactions also occur, inducing the formation non-equilibrium high temperature phases, such as TiO₂ anatase and rutile phases ^[22]. From the technological point of view, PEO shows several advantages over other techniques, *i.e.*: (i) processing time is one order of magnitude shorter compared to electrochemical anodization employed to synthesise TiO₂ nanotube arrays (5-10 min in PEO vs few hours in conventional anodization) and no annealing pre-treatment is needed; (ii) capital asset required for the fabrication and installation of an industrial plant is one order of magnitude lower than for vacuum deposition techniques; (iii) unlike conventional anodization and wet chemical methods, no crystallization post-treatment is required, since the as-grown TiO₂ coatings are already crystalline. Additionally, PEO is a well-established industrial process for aluminium and magnesium alloys surface treatment ^[22,23]; therefore, no serious plant design and energy consumption issues are foreseen.

Titanium dioxide films obtained by PEO exhibit sponge-like morphology, high hardness, good adhesion to the substrate and thermo-mechanical stability^[24–26]. Therefore, PEO TiO₂ films could provide high surface area and good electron transfer at the Ti/TiO₂ interface. Surprisingly, the photoelectrochemical activity of TiO₂ films obtained by PEO and their possible exploitation in solar-assisted water splitting has been hardly considered so far. In fact, PEO-prepared TiO₂ films are not even mentioned in recent reviews on the environmental applications of photoelectrocatalysis^[27–29].

In a previous study, some of the authors investigated the effect of the electrolyte temperature on the structure and photoelectrocatalytic (PEC) activity of TiO₂ films obtained by PEO in H₂SO₄ solutions and found that by lowering the electrolyte temperature from 25 to 0°C during the PEO treatment and by tuning the cell voltage, the incident photon-to-current efficiency (IPCE) under UV-C irradiation (254 nm) of the obtained photoactive layers increased from 11 to 82%^[12].

The aim of the present work is the validation of PEO as a valuable technique to produce TiO₂ photoanodes for photocatalytic water splitting. A systematic investigation has been performed aimed at determining how the PEO conditions affect the morphology, crystalline structure, and charge transfer properties of the obtained oxide layer, and at optimizing the PEO conditions to prepare high area TiO₂ electrodes for photocatalytic water splitting.

2. Results and discussion

TiO₂ electrodes were prepared by a single-step procedure based on PEO of titanium sheets, conducted at different cell potentials and processing times. They were labeled as X-Y, with X referring to the cell voltage (A = 100 V; B = 150 V; C = 180 V) and Y to the PEO processing time in seconds.

2.1 SEM, GD-OES and XPS analyses

Figure 1 shows a typical SEM surface and tilted fractured surface micrographs of the sample B-300. The oxide surface appears homogeneously porous, while the fracture surface shows a non-uniform porosity across the film thickness. As shown in **Figure S1** of the Supplementary Information, and in agreement with the literature ^[30,31], by increasing the anodization cell voltage from 100 V to 150 V or 180 V, the morphology of the porous layer evolved into a more interconnected and sponge-like structure. Based on ImageJ software analysis, the average pore size of samples A series varied from 124 ± 36 nm for sample A-60 to 148 ± 54 nm for A-900. In samples B series, the pore size increased from 316 ± 128 nm for B-30 to 472 ± 132 nm for B-300, and similarly the pore size of samples C changed from 225 ± 65 nm for C-10 to 361 ± 135 nm for C-90. Though these pore size values are rather scattered, their average value appears to be marginally affected by the anodization time, especially at low cell voltage. On the contrary, pore size is clearly affected by the applied cell voltage.

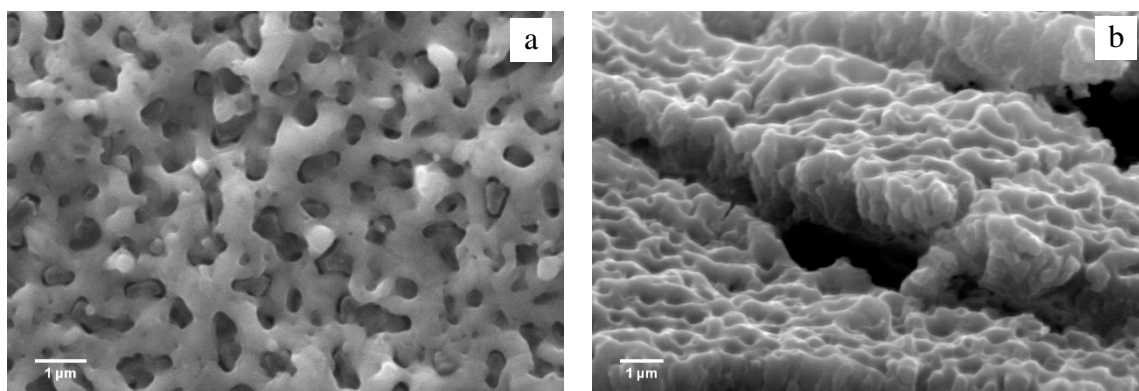


Figure 1. SEM micrographs of (a) the surface and (b) the fracture-section of sample B-300.

The in-depth GD-OES elemental analysis reported in **Figure 2** reveals that, in addition to the expected signals attributed to oxygen and titanium atoms, a signal corresponding to sulfur is evident in proximity of the TiO_2/Ti interface. This signal exhibits a wide tail towards the film surface, more evident at higher anodizing potentials. This effect could be attributed to the more intense and dense sparking activity occurring at higher anodization potential, inducing a more

pronounced remix of the locally melted oxide and favoring migration towards the film surface of sulfur-containing species initially included in the oxide.

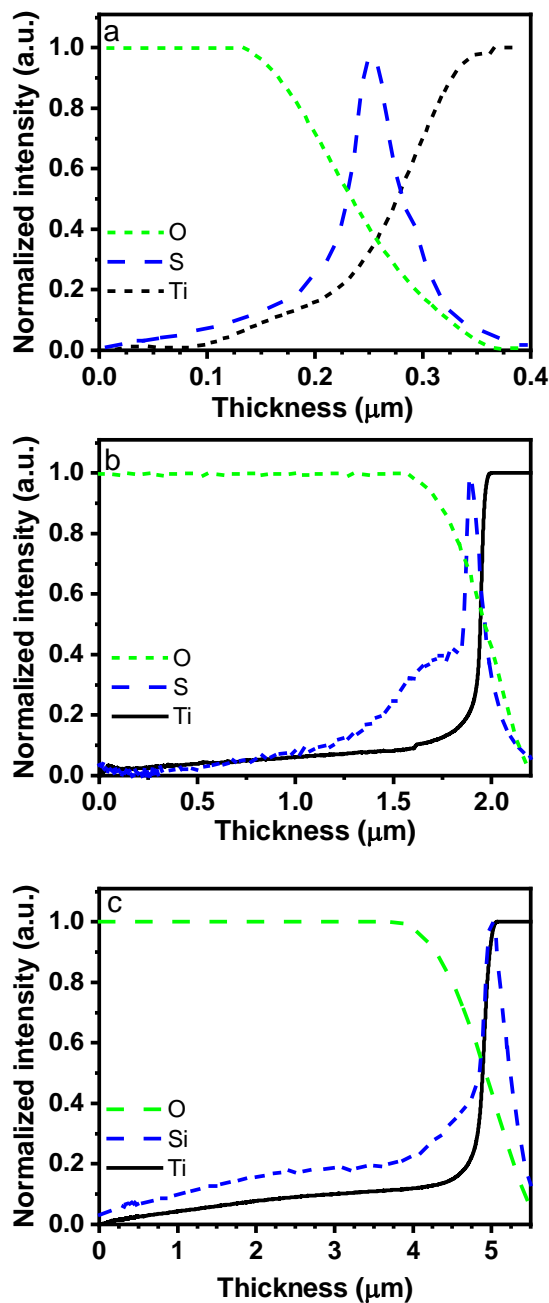


Figure 2. GD-OES in depth analysis for samples: (a) A-300, (b) B-90, and (c) C-90.

More information on sulfur species, incorporated into TiO_2 , was obtained by XPS analysis. The broad XPS survey scan shown in **Figure 3(a)** exhibits the photoemission signals expected from O, Ti, C and S. The C 1s signal is attributed to adventitious carbon, while the O 1s peak at 530

eV corresponds to oxygen bound to Ti^[32]. The narrow-scan spectrum around the S 2p binding energy (BE), shown in Figure 3(b), reveals the presence of a feature at 169.2 eV, compatible with the superposition of photoemission from both tetravalent S⁴⁺ and hexavalent S⁶⁺ sulfur (BE equal to 168.8 and 169.5 eV, respectively)^[33]. The strongest peak at 169.5 eV is usually assigned to SO₄⁻² species, such as sulfuric acid adsorbed on the TiO₂ surface^[34], likely arising from sulfuric acid solutions used for PEO. As for the tetravalent sulfur signal, S⁴⁺ species can be incorporated into TiO₂ either interstitially or at the Ti⁴⁺ lattice site^[35].

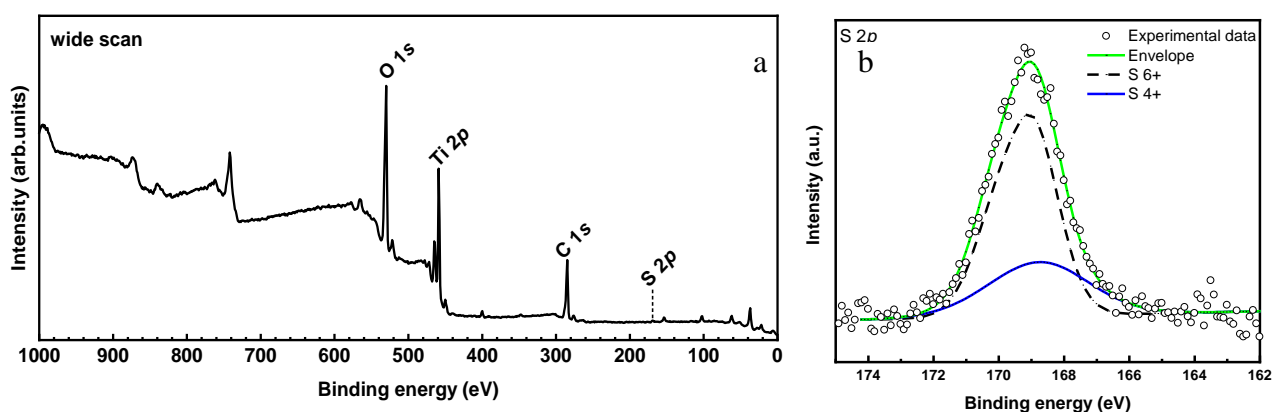


Figure 3. (a) XPS wide scan of sample C-5. The S peak is marked with a dashed line. (b) The S 2p signal at BE around 169.2 eV and its deconvolution.

2.2 Electrochemical surface area

Figure 4(a) shows the thickness of TiO₂ films as a function of the processing time at the three cell voltages (100 V, 150 V, and 180 V). Samples A were *ca* 300 nm thick regardless of the process duration, while the thickness of films B increased from 1 to 2.5 μ m with increasing processing time. As expected, the film thickness varied more significantly in samples C, namely from 1.5 μ m for C-10 up to *ca* 5 μ m for C-90.

Since electrode reaction rates and most double layer parameters are extensive quantities referred to the interface unit area, the surface area (SA) of the electrodes needs to be determined. In the

present study, SA was measured both in-situ and ex-situ. The in-situ measurement relies on the capacitance ratio of the porous photoelectrode in a model aqueous electrolyte with respect to that of the same oxide having an ideally flat surface. The electrochemical surface area (ECSA) of the electrode was measured at various cell voltages and processing times (Figure 4(b)). The following equations were applied [36]:

$$C_T = \frac{I}{\left(\frac{dE}{dt}\right)} \quad \text{Equation 1}$$

$$ECSA = \frac{C_T}{C^* \cdot A} \quad \text{Equation 2}$$

where C_T is the total capacitance (F), I is the current (A), dE/dt is the voltage scan rate ($V \cdot s^{-1}$), C^* is the specific capacitance ($F \cdot cm^{-2}$), A is the geometric area of the sample (cm^2), and ECSA is the electrochemical surface area per geometric area ($cm^2 \cdot cm^{-2}$). The main limitation of this method is the general assumption that the specific capacitance of oxides is $60 \mu F \cdot cm^{-2}$, regardless of the oxide composition and crystalline structure, and without considering the composition of the electrolyte in which the measurement is carried out. Since literature lacks in reporting a reference C^* value for titanium dioxide, for a more reliable evaluation of the ECSA, a smooth ($R_a = 20$ nm) TiO_2 film was prepared by annealing a mirror-polished titanium sheet in air at $300^\circ C$ for 24 h, and the corresponding capacitance was measured under the same experimental conditions as for the PEO TiO_2 films. The resulting capacitance value of $0.86 \mu F \cdot cm^{-2}$ was taken as specific capacitance C^* . Following this approach, ECSA values were in the range from $17 cm^2 \cdot cm^{-2}$ to $107 cm^2 \cdot cm^{-2}$, depending on the adopted PEO parameters (**Figure 4(b)**). Therefore, the porous morphology of the PEO TiO_2 induced an increase of the surface area of one to two orders of magnitude with respect to the geometric area of the electrode.

To validate the proposed approach, ex-situ measurements were also done for selected samples, based on the adsorption of probe gas molecules (N_2). The corresponding BET surface area values are in good agreement with ECSA values. For example, for sample B-300, the

electrochemical surface area per unit mass, calculated as the ratio between the total electrochemical surface area and the total mass of the sample, is $5.2 \text{ m}^2 \cdot \text{g}^{-1}$ and the BET surface area value is $6.3 \text{ m}^2 \cdot \text{g}^{-1}$. This slight discrepancy can be well accepted, considering that the two methods rely on different physical phenomena and that the pores accessible to the N_2 gas molecules are not necessarily accessible to anions/cations in electrolyte media.

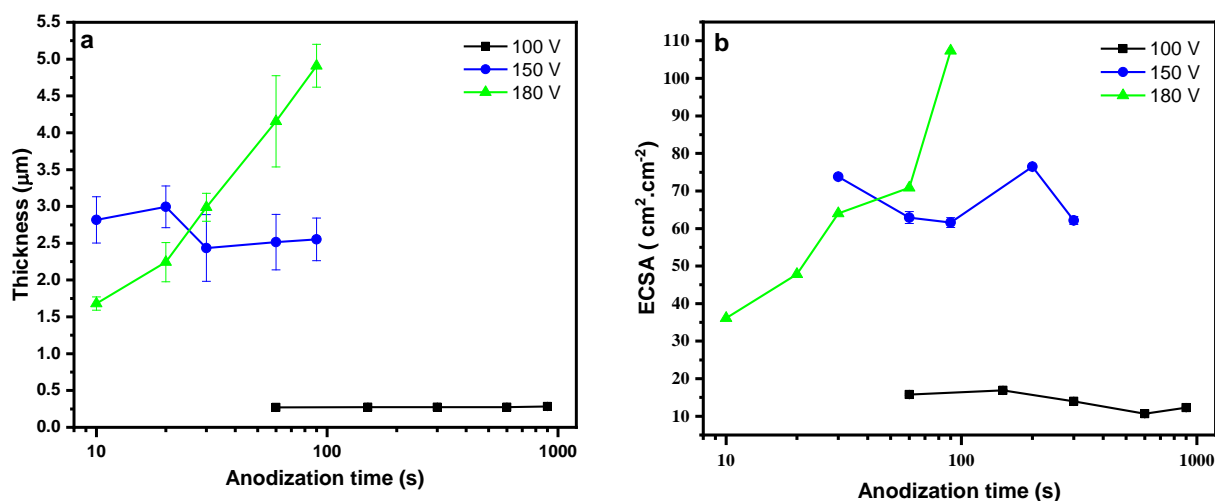


Figure 4. (a) Thickness and (b) ECSA of TiO_2 films obtained by PEO at different cell voltages and anodization times.

2.3 Electrochemical Impedance Spectroscopy

Figure 5 shows the Nyquist and Bode plots for some representative samples, prepared at three different cell voltages for different processing times (A-900, B-200, and C-90). Nyquist plots exhibit a typical semicircle shape. Bode plots reveal two different phase angle shapes, consisting in either a single peaked or a double peaked curve and corresponding to either one or two time constant electrodes, respectively. PEO TiO_2 might show a stratified structure consisting in a porous surface layer and a denser under-layer positioned at the Ti/TiO_2 interface [37–39]. In the present study, the electrodes prepared at 100 V show a single time constant, thus a single layer structure can be inferred, while the electrodes prepared at higher cell voltages

exhibit two time constants, suggesting a stratified structure. Accordingly, two different equivalent electrical circuits best fit the Electrochemical Impedance Spectroscopy (EIS) results.

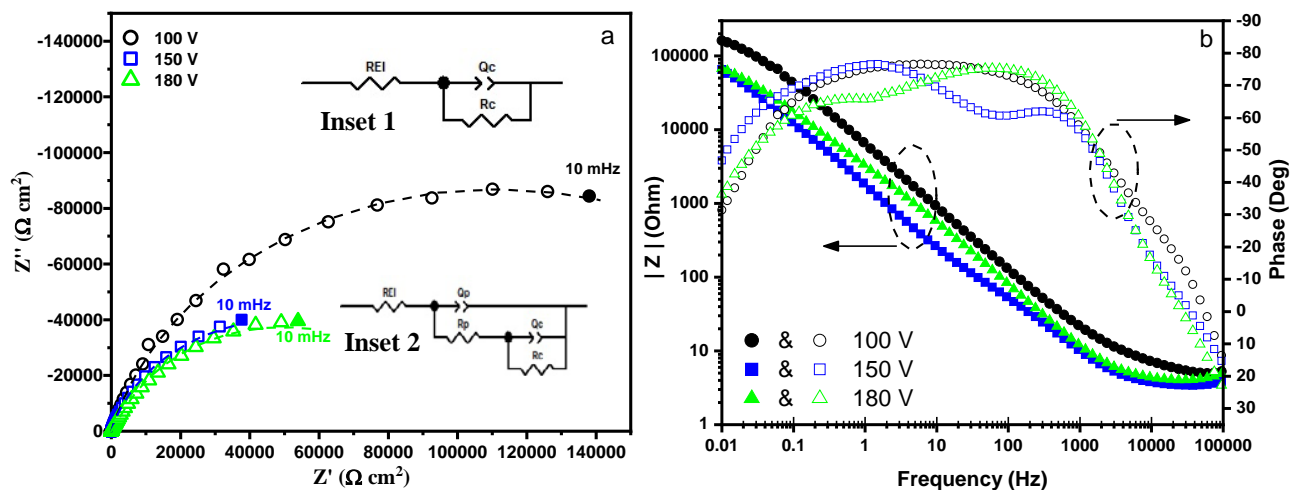


Figure 5. (a) Nyquist plots of experimental (symbols) and fitted (dashed lines) data for samples A-900, B-200 and C-90. The upper and lower insets are the corresponding electrical equivalent circuits. (b) Bode plots from the experimental data obtained on the same samples.

EIS results referring to electrodes obtained at 100 V were best fitted by the simplified Randles equivalent circuit shown in **Figure 6(a)** (inset 1). R_s is the series resistance accounting for all ohmic resistors, *i.e.* external contacts and wires, electrode sheet resistance, electrolyte resistance, interface resistance. As expected, similar R_s values were calculated for all specimens, although a slightly higher value was obtained for the electrode prepared at 100 V (Table 1). This discrepancy might be tentatively explained by a higher Ti/TiO₂ interface resistance. R_c represents the resistance of a more “compact” TiO₂ layer. For a more accurate fit, the constant phase element (CPE) was introduced in the circuit instead of a pure double layer capacitor (Q). The impedance of CPE is defined as $Z_{CPE} = 1/(j\omega)^n Q$, where n describes the degree of non-ideal behavior of CPE (unitless), Q represents the differential capacitance of the interface ($\text{F}\cdot\text{cm}^{-2}$) when n approaches 1, and $\omega = 2\pi f$ is the angular frequency (Hz).

EIS results referring to electrodes obtained at cell voltages of 150 and 180 V were well fitted by the equivalent circuit represented in Figure 5(a) (inset 2). In addition to the previous circuit

elements, two more elements were added, namely R_p and Q_p , representing the resistance and the differential capacitance, respectively, of an additional and possibly more porous TiO₂ layer. The obtained results are plotted in **Figure 6(b,c)** and reported in Table 1.

Though a comparison of the two models might not be straightforward, it should be emphasized that the sample A-900 exhibited the highest R_c value (222 kΩ.cm⁻²) despite its lower thickness. The resistance R_c decreased to 168 and 92 kΩ.cm⁻² for samples B-200 and C-90, respectively. This may suggest that the TiO₂ layer at the interface with the Ti substrate was less compact and/or thinner for higher cell voltages. Additionally, since XRD patterns show that the amount of rutile increased in films obtained at higher cell voltage (see section 3.5), the correspondingly lower R_c values may partially be explained by the lower dielectric constant of rutile relative to anatase^[40]. As expected, the resistance of the porous layer (R_p) rises with the PEO cell voltage, due to a higher thickness of the TiO₂ film.

The total effective capacitance per geometric area unit associated with the CPE was calculated following Hirschorn et al.^[41]:

$$C_{eff} = Q^{\frac{1}{n}} R_f^{(1-n)/n} \quad \text{Equation 3}$$

where n describes the degree of non-ideal behavior of CPE (unitless), Q is the differential capacitance of the interface (F.cm⁻²), R_f is the resistance either of the porous or of the compact layer (Ω.cm⁻²) and C_{eff} is the corresponding effective capacitance.

The values of effective capacitance of the porous layer ($C_{eff,p}$), of the compact layer ($C_{eff,c}$), the total effective capacitance (C_{eff}) and the total capacitance per geometric area unit (C_T/A) calculated to evaluate ECSA are reported in Table 1. The compact layers show higher C_{eff} than the porous layers. Interestingly, the total effective capacitance measured by EIS is in good agreement with the total capacitance per geometric area unit measured by Cyclic Voltammetry (CV). Indeed, sample B-200 has a C_{eff} value of 70.71 μF.cm⁻² (EIS) and a C_T/A value of 65.78

$\mu\text{F}\cdot\text{cm}^{-2}$ (CV). Similarly, for sample C-90 the C_{eff} and $C_{\text{T/A}}$ values were $96.99 \mu\text{F}$ and $92.34 \mu\text{F}$, respectively.

Therefore, based on EIS results the electrodes synthesized at higher potential have a double-layered structure consisting in a compact underlayer and a more porous surface layer with a 3D in-depth development [42], while the electrodes obtained at 100 V consist in a single more compact layer. The overall resistance of the electrodes decreases with the applied cell voltage, while the capacitance increases.

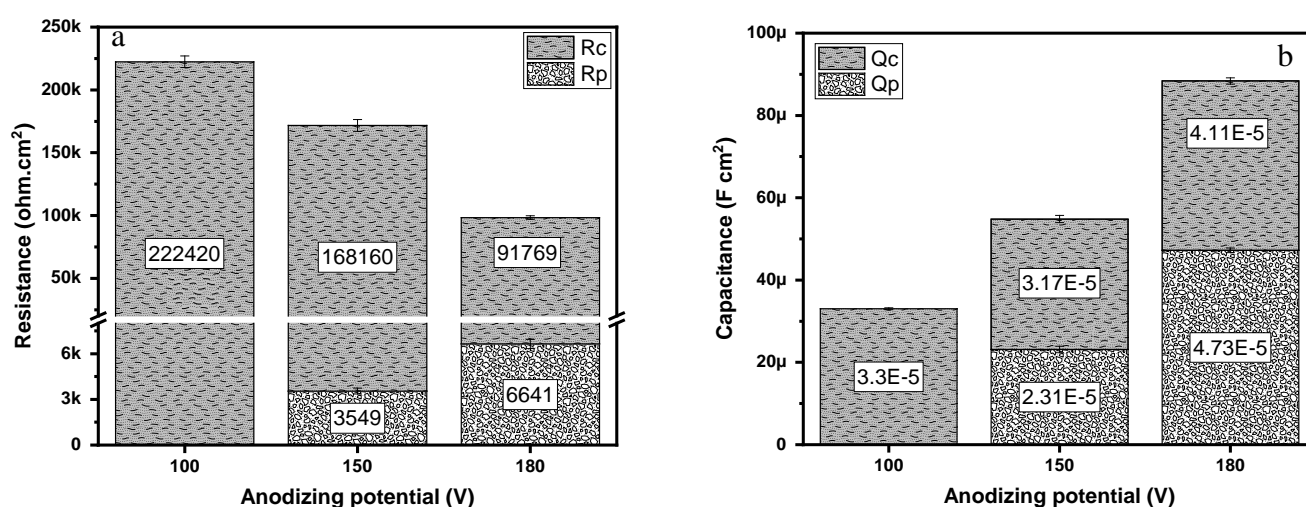


Figure 6. EIS data according to the proposed models: (a) resistance of the compact layer (R_c) and of the porous layer (R_p), (b) differential capacitance of the compact layer (Q_c) and of the porous layer (Q_p) for samples A-900, B-200 and C-90.

Table 1. EIS fitting values: ohmic resistance (R_s), degree of non-ideal behavior of porous layer (n_p) and compact layer (n_c), Pearson's chi-square test (χ^2), effective capacitance of the porous layer ($C_{\text{eff,p}}$) and of the compact layer ($C_{\text{eff,c}}$), total effective capacitance (C_{eff}). CV total capacitance per geometric area unit ($C_{\text{T/A}}$).

Sample	R_s ($\Omega \text{ cm}^2$)	n_p	n_c	χ^2	$C_{\text{eff,p}}$ ($\mu\text{F cm}^2$)	$C_{\text{eff,c}}$ ($\mu\text{F cm}^2$)	C_{eff} ($\mu\text{F cm}^2$)	$C_{\text{T/A}}$ ($\mu\text{F cm}^2$)
A-900	6.2	-	0.84	0.003	-	47.7	47.7	
B-200	3.9	0.74	0.72	0.001	9.9	60.8	70.7	65.8
C-90	3.9	0.87	0.8	0.001	39.7	57.3	97	92.3

2.4 Crystalline structure and band-gap determination

Figure S2 shows the XRD patterns of samples prepared at different cell voltages and anodization times. The reflections at $2\theta \approx 25.35^\circ$, 36.88° , 48.07° , and 55.11° were attributed to the anatase phase, the reflections at $2\theta \approx 27.44^\circ$, 36.09° , 41.25° , and 54.33° to the rutile phase, and the reflections at $2\theta \approx 35.06^\circ$, 38.40° , 40.15° , and 53.00° to the Ti substrate. XRD analysis evidences that all PEO-prepared TiO_2 films are crystalline, even though the presence of a minor amorphous component cannot be completely ruled out [43].

The weight percentage of anatase phase, obtained at the three cell voltages, as a function of anodization time is shown in **Figure 7(a)**. The predominant crystalline phase shifted from pure anatase to a mixture of anatase and rutile when the cell voltage changed from 100 V to 150 V or 180 V, respectively. This can be explained by considering that a higher discharge density at higher potentials induces a stronger local heating of the oxide film, which favors the anatase to rutile phase transformation. Furthermore, the phase composition did not vary with the anodization time at 100 V and 150 V, whereas at 180 V a phase transition from a mixture of anatase and rutile to almost pure rutile occurred during anodization, as reported also by others [13].

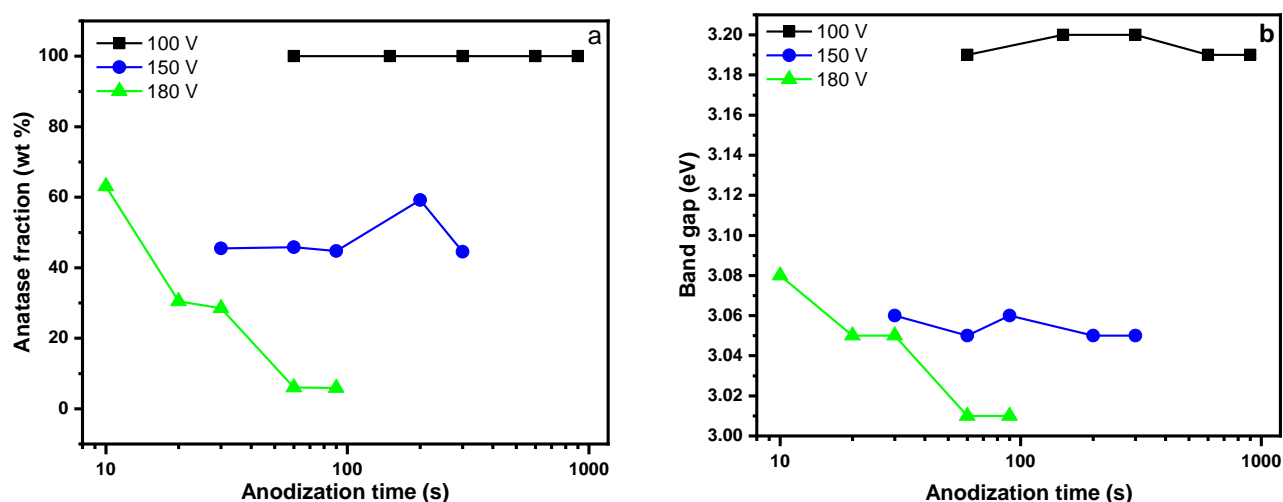


Figure 7. (a) Anatase fraction in the TiO_2 layer as a function of the anodization time at the three cell voltages. (b) Band-gap values of TiO_2 obtained at different cell voltages.

The UV-Vis-NIR diffuse reflectance spectra of some representative samples are shown in **Figure S3**, as Tauc-plots of the Kubelka–Munk transform. The spectra relative to the PEO-produced TiO₂ films obtained at 100 V showed fringe perturbations in the visible region, due to the low thickness of the films, causing interference of the waves reflected at the top and bottom surface. In such case, the band gap could be determined by extrapolating to zero the linear fit of $(\alpha hv)^{\frac{1}{2}}$ versus the photon energy ^[44]. The calculated band gap values of all TiO₂ layers obtained at different anodization potentials and processing times are plotted in Figure 7(b).

Samples prepared at 100 V have band gap values of ≈ 3.2 eV, in agreement with literature values for pure anatase ^[45]. The band gap trend of samples obtained at 150 V and 180 V follows their phase composition ^[43]. In particular, when the crystalline structure consists of an anatase and rutile mixture, the band gap is ≈ 3.06 eV, while it decreases to ≈ 3.01 eV where rutile is the largely predominant phase.

2.5 Incident Photon to Current Efficiency (IPCE)

The photocurrent density values measured with the TiO₂ electrodes prepared at different cell voltages and anodization times are plotted in **Figure S4** as a function of the incident wavelength under two experimental conditions, *i.e.*, without any applied bias and with a 0.6 V vs. SCE applied bias. Moreover, the corresponding light power is also reported on the right y-axis of each figure. TiO₂ films prepared at 100 and 180 V (long processing times) exhibit a Gaussian-shaped curve, while a bimodal distribution is observed in electrodes obtained at cell voltages of 150 and 180 V (short processing times). This distinct difference reflects the crystalline structure of the TiO₂ film, which is either almost mono phase (anatase or rutile) or an anatase and rutile mixture. In fact, according to the literature ^[46,47], the absorption peaks around 325 nm and 380 nm are attributed to the anatase and rutile phases, respectively. By applying a 0.6 V

(vs. SCE) bias the photocurrent raises by 50 to 300 % depending on the wavelength (Figure S4(b,d,f)), irrespectively of the anodization potential and time adopted in the electrode synthesis. This might be a consequence of both a more efficient extraction of promoted electrons from the conduction band and a decreased electron-hole recombination. On average, the application of the anodic bias was more beneficial for samples B prepared at 150 V.

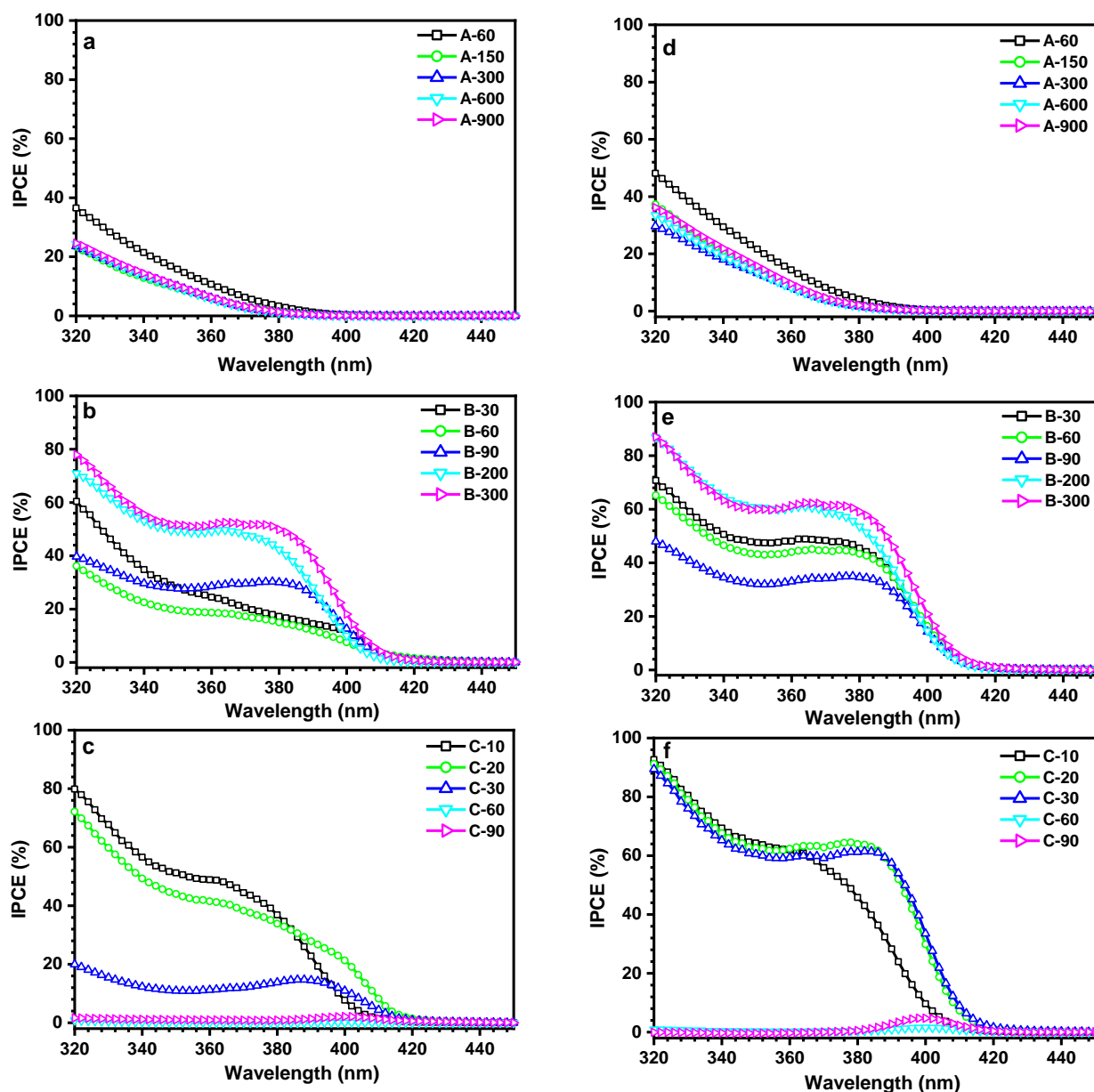


Figure 8. IPCE curves measured with TiO_2 electrodes obtained at (a,d) 100 V, (b,e) 150 V and (c,f) 180 V cell voltages with the anodization times indicated in the panels, (a,b,c) in the absence of applied bias and (e,f,g) under 0.6 V vs. SCE.

Based on the photocurrent data reported in Figure S4, the corresponding IPCE curves were calculated according to Equation 5 and plotted in **Figure 8**. Depending on the incident

wavelength and cell voltage, the IPCE values are relatively high even without any applied bias (80%), reaching a 94% value under 0.6 V vs. SCE, which far exceeds literature data for TiO₂ films [48–50]. Furthermore, it is worth underlining that IPCE values reported in the literature for undoped TiO₂ are below 55% and refer to about 1 cm² surface area electrodes, whereas our IPCE values were obtained with a much larger surface area electrodes (10 cm²), which can be obtained by PEO in less than 10 min processing.

The IPCE onset of samples mostly consisting in anatase (samples A) is 390 nm, in agreement with the calculated band gap. Similarly, the IPCE onset of the samples B and C is around 410 nm corresponding to the band gap of the rutile phase. Furthermore, the IPCE curves are also affected by the TiO₂ film thickness and surface area. Higher IPCE values should be expected for electrodes having higher surface area and their thickness should be optimized also in consideration of electron trapping and charge recombination phenomena occurring to a larger extent in thicker layers [51].

Samples A are relatively thin and this results in low electrochemical surface area and significant reflection of the incident light, as demonstrated by the fringes of the spectra shown in Figure S3. Thus, the IPCE values are limited to about 50%. On the other hand, in the case of samples C with longer processing times and consisting of almost pure rutile, the beneficial effect of a relatively higher ECSA was significantly scaled down by the higher probability of electron-hole recombination due to their larger thickness. Correspondingly, the IPCE was 5% or even lower. Based on these results, it can be concluded that the optimum thickness for TiO₂ films was 2 – 2.5 μm.

2.6 Separate production of H₂ and O₂

Linear sweep voltammetry tests and separate H₂ and O₂ production measurements under simulated solar light (AM 1.5 G) were performed with selected photoactive electrodes, chosen among those showing the highest IPCE per each processing voltage and phase composition,

i.e., pure anatase (sample A-60), pure rutile (sample C-90) and a mixture of the two phases (sample B-300). **Figure 9** shows the photocurrent responses as a function of the applied bias under dark conditions, under continuous irradiation (light) and under chopped irradiation (dark-light). In agreement with data shown in Figure S4, the photocurrent of the selected electrode prepared at 150 V was much higher compared to the others, due to beneficial combination of the anatase and rutile phases and possibly for its suitable thickness.

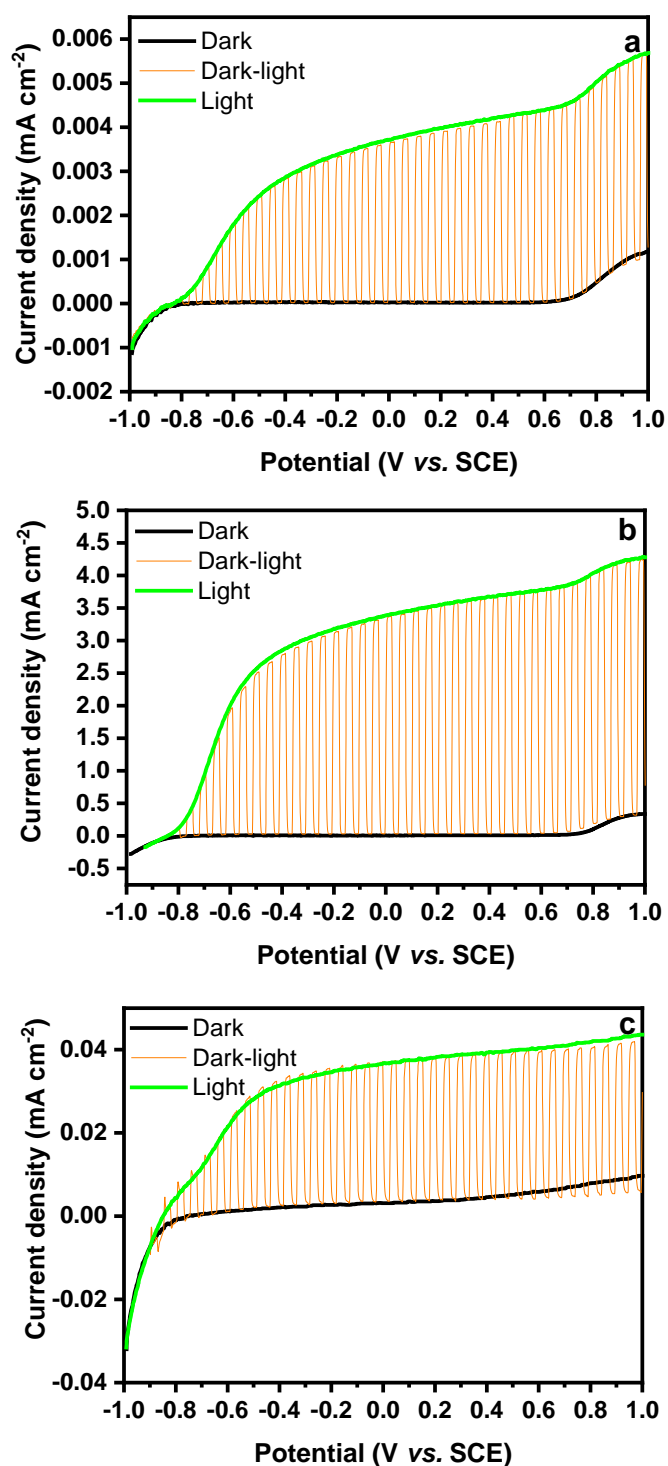
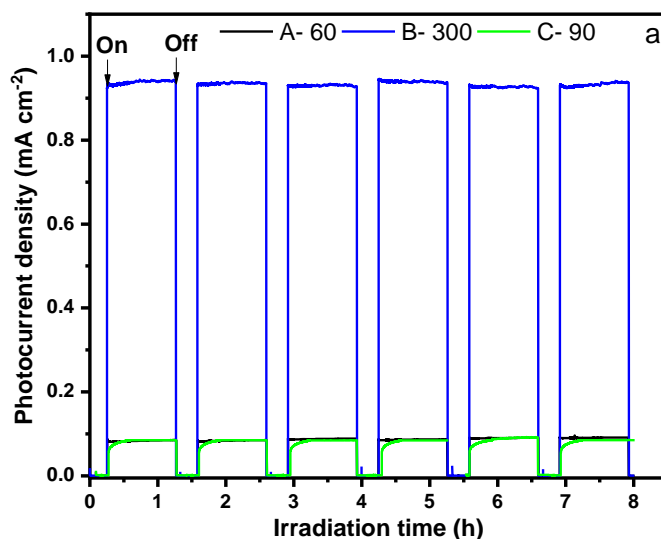


Figure 9. Linear sweep voltammetry curves recorded with selected electrodes: (a) A-60; (b) B-300, and (c) C-90, in 1.0 M NaOH with a scan rate of 5 mV s⁻¹. Photocurrent responses in the dark (black line), under chopped light (dark-light, orange line) and continuous irradiation (light, green line).

Figure 10 (a) shows the photocurrent density during the separate production of H₂ and O₂ under discontinuous simulated solar light irradiation for 6 h. The three electrodes showed a stable

performance over time, as demonstrated by the stability of the photocurrent density during the test, with sample B-300 outperforming the others, as expected. Figure 10(b) shows the amount of collected H₂ and O₂ gases as a function of the irradiation time for the same sample. The theoretical amount in moles of evolved H₂ and O₂ expected on the basis of the total charge flowing during the test is also shown. While the amount of evolved H₂ is in agreement with the theoretical value, the amount of O₂ is below the expected value. Correspondingly, the experimental H₂:O₂ molar ratio approached the stoichiometric value of 2 only after 5 h. This discrepancy might be attributed to the relatively high solubility of oxygen in the electrolyte with respect to hydrogen. After 5 h the apparent delay in O₂ production was recovered, possibly because the electrolyte reached O₂ saturation. However, the presence of hydrogen peroxide as water oxidation intermediate cannot be ruled out. Hydrogen peroxide is rather unstable in NaOH and would decompose to O₂ possibly contributing to the observed O₂ production delay. The H₂ production rate was 0.17 mmol h⁻¹, in line with previous findings on TiO₂ nanotube array electrodes tested using the same experimental set-up^[46].



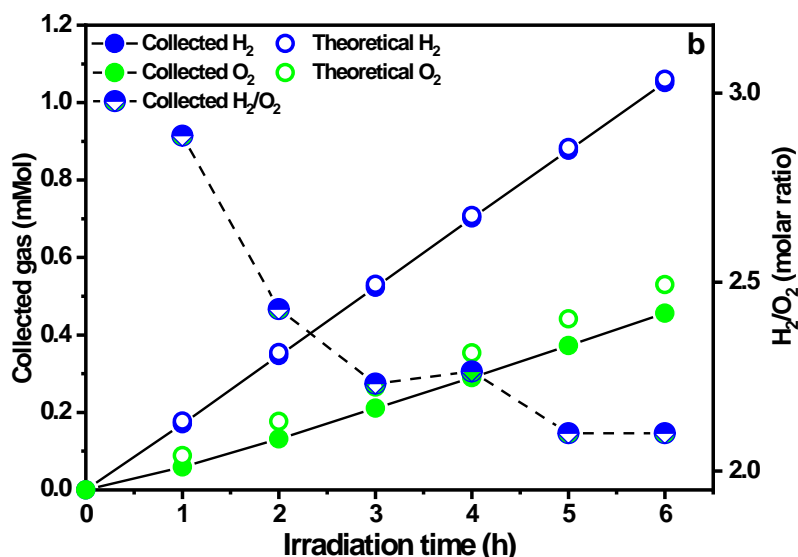


Figure 10. (a) Photocurrent density during H₂ and O₂ separate production under irradiation (AM 1.5 G, 100 mW.cm⁻²) for the three selected TiO₂ electrodes, (b) left ordinate: H₂ (blue) and O₂ (green) gases effectively collected under irradiation (full symbols) together with their theoretical values (empty symbols; right ordinate: experimental H₂/O₂ molar ratio (blue-green symbols).

3. Conclusion

This work represents the first comprehensive investigation and testing of large area TiO₂ (10-18 cm²) electrodes obtained by Plasma Electrolytic Oxidation for photocatalytic water splitting. The peculiar porous and homogenous morphology induced by PEO is beneficial for the operation of the electrode in photocatalysis. Indeed, the sponge-like structure obtained under higher cell voltages leads to a two orders of magnitude larger electrochemical surface area of the electrodes with respect to their geometric surface area. Correspondingly, the electrodes consisting of a single compact layer if prepared at 100 V, at higher voltages (150-180 V) develop a two-layer structure with a compact layer at the titanium interface and a thick porous layer on the oxide electrolyte interface. At higher cell voltages the compact layer becomes either thinner or less compact or both, while the porous layer becomes thicker, thus decreasing the overall resistance of the electrode and increasing the total capacitance. The as-prepared films are crystalline, with the phase composition tunable with the anodizing potential, pure anatase and almost pure rutile being the predominant phases produced at 100 V and 180 V for longer processing times, respectively, while a mixture of anatase and rutile is obtained at intermediate

cell voltage. This is reflected by the shape of the photocurrent vs. wavelength curves, the electrodes consisting in a mixture of anatase and rutile exhibiting bimodal photocurrent vs. wavelength curve and maximum IPCE values far exceeding those reported in literature for undoped TiO₂ films. The electrodes produce a stable photocurrent response under both continuous and chopped simulated solar light and a H₂ production rate in line that obtained with TiO₂ nanotube array electrodes. Thus, Plasma Electrolytic Oxidation is a promising technique for preparation of large-area TiO₂-based photoelectrodes for photocatalytic water splitting, being a single-step process which does not require pre- or post-treatments of the titanium substrate, lasts only few minutes, is already in use in the field of surface treatments of other valve metals and is therefore easily scalable at the industrial level.

4. Experimental section

4.1 Preparation of TiO₂ photoanodes

TiO₂ films were prepared by a single-step procedure based on PEO of commercially pure (Grade I) titanium sheets, without any pre and post treatment. PEO was conducted in DC mode at different cell potentials and processing times, namely at 100 V (60, 150, 300, 600, and 900 s), 150 V (30, 60, 90, 200, and 300 s), and 180 V (10, 20, 30, 60, and 90 s). A titanium sheet with 18 cm² exposed area was used as the anode, while the cathode was a titanium mesh. The electrolyte was a 1.5 M H₂SO₄ aqueous solution with a total volume of 1 L. During PEO, the electrolyte temperature was set at -5 °C by means of a cryostat (HAAKE D10, Thermo Electron Corp., Karlsruhe, Germany). Possible shift of utmost 5 °C from the set point was unavoidable at 180 V anodization potential. After PEO, the samples were rinsed with water and dried in an air stream. All samples were prepared in duplicate. The obtained materials were labeled as X-Y with X referring to the cell voltage (A = 100 V; B = 150 V; C = 180 V) and Y referring to the PEO processing time in seconds.

4.2 Characterization of TiO₂ photoanodes

The surface morphology of the TiO₂ films was investigated by scanning electron microscopy (SEM, Zeiss EVO 50, Carl Zeiss Jena GmbH, Jena, Germany). Their thickness was obtained either by spectrophotometry using a spectrophotometer (CM-2600 d, Konika Minolta Inc., Tokyo, Japan) (samples A) or by means of cross-section SEM images (samples B and C). The surface average roughness (R_a) was estimated by Atomic Force Microscopy (AFM) sampling an area of 5 μm x 5 μm with a AFM Solver Pro apparatus (NT-MDT Spectrum Instruments, Moscow, Russia) operating in contact scanning mode.

The in-depth elemental composition of the TiO₂ films was assessed by Glow Discharge Optical Emission Spectrometry (GD-OES) using a Spectrum GDA750 analyzer (SPECTRO Analytical Instruments Inc., Kleve, Germany) operated at 700 V in argon atmosphere at 230 Pa.

X-ray photoemission spectroscopy (XPS) data were acquired with a Phoibos 150 hemispherical analyzer from SPECS GmbH (Berlin, Germany), by exciting the electrons with a Mg-K α source ($h\nu = 1253.6$ eV). The spectrometer was housed in a home-built vacuum system described elsewhere^[52], kept in ultra-high vacuum conditions (base pressure in the low 10⁻⁸ Pa). Possible charging effects were accounted for by setting at 285 eV the peak of adventitious carbon^[53].

X-ray diffraction (XRD) patterns were recorded by a PW1830 diffractometer (Malvern Panalytical Ltd, Malvern, UK and Almelo, The Netherlands) operating at 40 kV voltage and 40 mA filament current. The spectra were acquired at the scanning rate of 2.5° min⁻¹ with CuK α_1 radiation in the 20 – 60° 2 θ range. The XRD patterns were indexed according to the powder diffraction files released by the International Center for Diffraction Data (U.S.) for titanium (PDF 44-1294), anatase (PDF 21-1272) and rutile phases (PDF 21-1276). The weight fraction of anatase (f_A) was calculated according to Equation 4^[54], where I_R is the intensity of the (110) rutile reflection and I_A is the intensity of the (101) anatase reflection.

$$f_A = \frac{1}{\left(1 + 1.26 \frac{(I_R)}{(I_A)}\right)} \%$$

Equation 4

UV-Vis-NIR diffuse reflectance spectra (DRS) were recorded in the 220–2600 nm range with a UV3600 Plus spectrophotometer from Shimadzu Corp. (Kyoto, Japan) equipped with an ISR-603 integrating sphere. The band gap was calculated based on the UV-Vis reflectance spectra after Kubelka-Munk conversion using the Tauc plot method ^[55].

The surface area was evaluated following two different approaches. The Brunauer-Emmett-Teller (BET) surface area was evaluated by low temperature (77 K) adsorption of N₂ as molecular gas probe, using a Tristar II 3020 apparatus (Micromeritics Instruments Corp., Norcross, U.S.) after outgassing the samples at 80 °C for 24 h under nitrogen flux. The nitrogen isotherms were analyzed using the BET theory from the instrumental software (Version 1.03). The electrochemical surface area (ECSA) was determined based on the electrochemical capacitance of the TiO₂ films using cyclic voltammetry (CV) in a potential window of ± 50 mV centered at open circuit potential (OCP), to avoid faradic responses ^[56]. CV measurements were conducted in a 1.0 M NaOH solution by performing five CV cycles at different scan rates (50, 100, 200, 300, and 400 mV s⁻¹). The average capacitive currents measured in the middle of the potential range were plotted as a function of the potential sweep rates.

Electrochemical Impedance Spectroscopy (EIS) measurements were performed in the dark and in 1.0 M NaOH aqueous solutions at the OCP of each specimen. The amplitude perturbation was 10 mV and the frequency ranged from 300 kHz to 10 mHz using a ModuLab® XM ECS high-performance potentiostat/galvanostat system (Solartron Analytical XM PSTAT 1 MS/s, Ametek Inc., Berwyn, U.S.). The instrument was coupled with a frequency response analyzer (Solartron Analytical, XM FRA 1MHz, Ametek Inc., Berwyn, U.S.) for AC measurements. The EIS results were fitted with a Randles-type equivalent circuit with the Zview software.

The photocurrent density was measured in a 1.0 M NaOH aqueous solution using an optical bench equipped with a 300 W Xe lamp (Lot-qd, Quantum Design Europe GmbH, Darmstadt,

Germany), a monochromator (Omni- λ 150, Quantum Design Europe GmbH, Darmstadt, Germany), a shutter (SC10, Thorlabs Inc., Newton, U.S.), and a homemade three electrode two compartment Plexiglas cell together with an optical Pyrex glass window. A TiO₂ photoelectrode with an irradiated area of 10 cm² was used as working electrode, a 25 × 25 mm² platinum foil and a saturated calomel electrode (SCE) were used as counter and reference electrodes, respectively. Electrochemical measurements were conducted at room temperature on both biased and unbiased TiO₂ photoelectrodes using a Amel, mod. 2549 potentiostat/galvanostat and a DMM4040 digital multimeter from Tektronix, Beaverton, U.S. The incident wavelength values ranged from 250 nm to 450 nm with a 2 nm step and a 4 s per step dwell time. The incident light power was measured using a calibrated Thorlabs S130VC photodiode connected to a power meter (PM200, Thorlabs Inc., Newton, U.S.) placed at exactly the same distance as the TiO₂ electrode, with the Pyrex window in between to account for the transmittance of the cell window. The Incident Photon to Current Efficiency (IPCE) at each wavelength was calculated using the following equation:

$$IPCE(\%) = \frac{h * c}{e} * \frac{I}{P * \lambda} \quad \text{Equation 5}$$

where h (kg.m².s⁻¹) is the Planck constant, c (m.s⁻¹) is the speed of light, e (C) is the electron charge, I (A.m⁻²) is the steady-state photocurrent density, P (W.m⁻²) is the light intensity and λ (m) is the incident wavelength.

4.3 Photo(electro)catalytic water splitting tests

Linear sweep voltammetry tests under simulated solar light (AM 1.5 G) were carried out in 1.0 M NaOH under a -1.0 to +1.0 V vs. SCE applied bias range. The TiO₂ photoanodes were tested in a two-compartment photocatalytic Plexiglas cell described elsewhere^[57], including a Nafion 117 cation exchange membrane to allow separate evolution of hydrogen and oxygen from the aqueous solutions. In each experiment, a TiO₂ photoanode having a geometrical area of 10 cm²

and a SCE reference electrode were immersed in a 1.0 M NaOH solution, while a Pt cathode was immersed in a 0.5 M H₂SO₄ solution. The three electrodes were connected to an potentiostat/galvanostat (model 2549 from Amel S.r.l., Milano, Italy) for chronoamperometric measurements while applying an electrical bias of 0.6 V vs. SCE to the working electrode. The photoanode was illuminated through a Pyrex glass optical window by an AM 1.5 G irradiation source at incident power density of 100 mW.cm⁻².

The H₂ and O₂ gases evolved during the tests were collected in two graduated burettes surmounting the two compartments of the cell and previously filled with the electrolyte solution. The volume of produced gas was measured every 60 min by the displacement of the liquid in the burettes after temporarily shutting down the light. Each photoelectrode was tested for 6 h.

Supporting Information

Supporting Information is available from the author.

Acknowledgments

The authors acknowledge Dr. Antonello Vincenzo, Dr. Maksim Bahdanchyk and Dr. Mazdak Hashempour Igderi, Department of Chemistry, Materials and Chemical Engineering of Politecnico di Milano, for their support in the analysis of EIS results; Dr. Mariangela Longhi, Department of Chemistry, University of Milano, for BET tests; Dr. Gianlorenzo Bussetti and Dr. Alberto Calloni, Department of Physics of Politecnico di Milano, for the XPS analysis and data interpretation. The use of instrumentation purchased through the SmartMatLab project, Fondazione Cariplo grant 2013-1766, is also gratefully acknowledged. This work was partially funded by the MIUR PRIN 2015K7FZLH SMARTNESS project and the MIUR PRIN 20173397R7 MULTI-e project.

Reference:

- [1] J. Garche, *Encyclopedia of Electrochemical Power Sources*; 2009.
- [2] S. Shen, J. Chen, M. Wang, X. Sheng, X. Chen, X. Feng, S. S. Mao, *Prog. Mater. Sci.* **2018**, 98, 299.
- [3] S. Franz, D. Perego, O. Marchese, M. Bestetti, *J. Water Chem. Technol.* **2015**, 37, 108.

- [4] M. C. Collivignarelli, A. Abbà, M. Carnevale Miino, H. Arab, M. Bestetti, S. Franz, *J. Hazard. Mater.* **2019**, 121668.
- [5] S. Murgolo, S. Franz, H. Arab, M. Bestetti, E. Falletta, G. Mascolo, *Water Res.* **2019**, 164.
- [6] S. B. Patil, P. S. Basavarajappa, N. Ganganagappa, M. S. Jyothi, A. V. Raghu, K. R. Reddy, *Int. J. Hydrogen Energy* **2019**, 44, 13022.
- [7] P. S. Basavarajappa, S. B. Patil, N. Ganganagappa, K. R. Reddy, A. V. Raghu, C. V. Reddy, *Int. J. Hydrogen Energy* **2020**, 45, 7764.
- [8] S. Franz, E. Falletta, H. Arab, S. Murgolo, M. Bestetti, G. Mascolo, *Catalysts* **2020**, 10, 169.
- [9] G. L. Chiarello, C. Tealdi, P. Mustarelli, E. Selli, *Materials (Basel)*. **2016**, 9.
- [10] M. Bestetti, D. Sacco, M. F. Brunella, S. Franz, R. Amadelli, L. Samiolo, *Mater. Chem. Phys.* **2010**, 124.
- [11] M. Bestetti, S. Franz, M. Cuzzolin, P. Arosio, P. L. Cavallotti, *Thin Solid Films* **2007**, 515.
- [12] S. Franz, D. Perego, O. Marchese, A. Lucotti, M. Bestetti, *Appl. Surf. Sci.* **2016**, 385, 498.
- [13] L. K. Mirelman, J. A. Curran, T. W. Clyne, *Surf. Coatings Technol.* **2012**, 207, 66.
- [14] S. Franz, H. Arab, A. Lucotti, C. Castiglioni, A. Vincenzo, F. Morini, M. Bestetti, *Catalysts* **2020**.
- [15] Z. Yao, F. Jia, S. Tian, C. Li, Z. Jiang, X. Bai, *ACS Appl. Mater. Interfaces* **2010**, 2, 2617.
- [16] T. Umebayashi, T. Yamaki, S. Yamamoto, A. Miyashita, S. Tanaka, T. Sumita, K. Asai, *J. Appl. Phys.* **2003**, 93, 5156.
- [17] J.-H. Lee, J.-I. Youn, Y.-J. Kim, I.-K. Kim, K.-W. Jang, H.-J. Oh, *Ceram. Int.* **2015**, 41, 11899.
- [18] M. S. Vasilyeva, V. S. Rudnev, A. A. Sergeev, K. A. Sergeeva, A. V. Nepomnyaschiy, A. Y. Ustinov, A. A. Zvereva, K. N. Kilin, S. S. Voznesenskiy, *Orig. Russ.* **2017**, 53, 532.
- [19] Z. Yao, F. Jia, Y. Jiang, C. X. Li, Z. Jiang, X. Bai, *Appl. Surf. Sci.* **2010**, 256, 1793.
- [20] R. Vasilić, S. Stojadinović, N. Radić, P. Stefanov, Z. Dohčević-Mitrović, B. Grbić, *Mater. Chem. Phys.* **2015**, 151, 337.
- [21] L. Wan, J. F. Li, J. Y. Feng, W. Sun, Z. Q. Mao, *Chinese J. Chem. Phys.* **2008**, 21.
- [22] A. L. Yerokhin, X. Nie, A. Leyland, A. Matthews, S. J. Dowey, *Plasma electrolysis for surface engineering*; 1999; Vol. 122.
- [23] F. C. Walsh, C. T. J. Low, R. J. K. Wood, K. T. Stevens, J. Archer, A. R. Poeton, A. Ryder, *Trans. IMF* **2009**, 87, 122.
- [24] N. B. Kondrikov, A. S. Lapina, A. K. Runov, G. I. Marinina, *Russ. J. Gen. Chem.* **2018**, 88, 1318.
- [25] P. Huang, F. Wang, K. Xu, Y. Han, *Surf. Coatings Technol.* **2007**, 201, 5168.
- [26] F. Jin, P. K. Chu, K. Wang, J. Zhao, A. Huang, H. Tong, *Mater. Sci. Eng. A* **2008**, 476, 78.
- [27] S. Garcia-Segura, E. Brillas, Applied photoelectrocatalysis on the degradation of organic pollutants in wastewaters. *J. Photochem. Photobiol. C Photochem. Rev.* **2017**, 31, 1–35.
- [28] G. G. Bessegato, T. T. Guaraldo, J. F. de Brito, M. F. Brugnera, M. V. B. Zanoni, Achievements and Trends in Photoelectrocatalysis: from Environmental to Energy Applications. *Electrocatalysis* **2015**.
- [29] V. Augugliaro, G. Camera-Roda, V. Loddo, G. Palmisano, L. Palmisano, J. Soria, S. Yurdakal, **2015**.
- [30] R. H. U. Khan, A. L. Yerokhin, X. Li, H. Dong, A. Matthews, *Surf. Eng.* **2014**, 30,

- 102.
- [31] Z. Yao, F. Jia, Y. Jiang, C. Li, Z. Jiang, X. Bai, *Appl. Surf. Sci.* **2010**, 256, 1793.
- [32] N. C. Saha, H. G. Tompkins, *J. Appl. Phys.* **1992**.
- [33] Z. Topalian, G. A. Niklasson, C. G. Granqvist, *ACS Appl. Mater. Interfaces* **2012**, 4, 34.
- [34] L. K. Randeniya, A. A. B. Murphy, A. I. C. Plumb, .
- [35] T. Ohno, M. Akiyoshi, T. Umebayashi, K. Asai, T. Mitsui, M. Matsumura, *Appl. Catal. A Gen.* **2004**, 265, 115.
- [36] R. Boggio, A. Carugati, S. Trasatti, *J. Appl. Electrochem.* **1987**, 17, 828.
- [37] M. Montazeri, C. Dehghanian, M. Shokouhfar, A. Baradaran, *Appl. Surf. Sci.* **2011**, 257, 7268.
- [38] S. Gowtham, T. Arunnellaiappan, N. Rameshbabu, *Surf. Coat. Technol.* **2016**, 301, 63.
- [39] S. Lederer, P. Lutz, W. Fürbeth, *Surf. Coatings Technol.* **2018**, 335, 62.
- [40] J. Y. Kim, H. S. Jung, J. H. No, J. R. Kim, K. S. Hong, *J. Electroceramics* **2006**, 16, 447.
- [41] B. Hirschorn, M. E. Orazem, B. Tribollet, V. Vivier, I. Frateur, M. Musiani, *Electrochim. Acta* **2010**, 55, 6218.
- [42] M. R. Bayati, F. Golestani-Fard, A. Z. Moshfegh, *Appl. Surf. Sci.* **2010**, 256, 4253.
- [43] A. E. R. Friedemann, K. Thiel, U. Haßlinger, M. Ritter, T. M. Gesing, P. Plagemann, *Appl. Surf. Sci.* **2018**, 443, 467.
- [44] S. Daviosdóttir, K. Dirscherl, S. Canulescu, R. Shabadi, R. Ambat, *RSC Adv.* **2013**, 3, 23296.
- [45] H. Tang, F. Lévy, H. Berger, P. E. Schmid, *Phys. Rev. B* **1995**.
- [46] G. L. Chiarello, A. Zuliani, D. Ceresoli, R. Martinazzo, E. Selli, *ACS Catal.* **2016**.
- [47] Y. Murata, S. Fukuta, S. Ishikawa, S. Yokoyama, *Sol. Energy Mater. Sol. Cells* **2000**, 62, 157.
- [48] H. Wu, Z. Zhang, *Int. J. Hydrogen Energy* **2011**, 36, 13481.
- [49] Q. Kang, J. Cao, Y. Zhang, L. Liu, H. Xu, J. Ye, *J. Mater. Chem. A* **2013**, 1, 5766.
- [50] C. J. Lin, Y. H. Yu, Y. H. Liou, *Appl. Catal. B Environ.* **2009**, 93, 119.
- [51] J. Krýsa, M. Keppert, G. Waldner, J. Jirkovský, In *Electrochimica Acta*; 2005.
- [52] G. Berti, A. Calloni, A. Brambilla, G. Bussetti, L. Duò, F. Ciccacci, *Rev. Sci. Instrum* **2014**, 85, 73901.
- [53] A. Galenda, F. Visentin, R. Gerbasi, S. Battiston, N. El Habra, *Water. Air. Soil Pollut.* **2016**.
- [54] R. A. Spurr, H. Myers, *Anal. Chem.* **1957**, 29, 760.
- [55] A. B. Murphy, *Sol. Energy Mater. Sol. Cells* **2007**, 91, 1326.
- [56] S. Trasatti, O. A. Petrii, *J. Electroanal. Chem.* **1992**, 327, 353.
- [57] E. Selli, G. L. Chiarello, E. Quartarone, P. Mustarelli, I. Rossetti, L. Forni, *Chem. Commun.* **2007**.

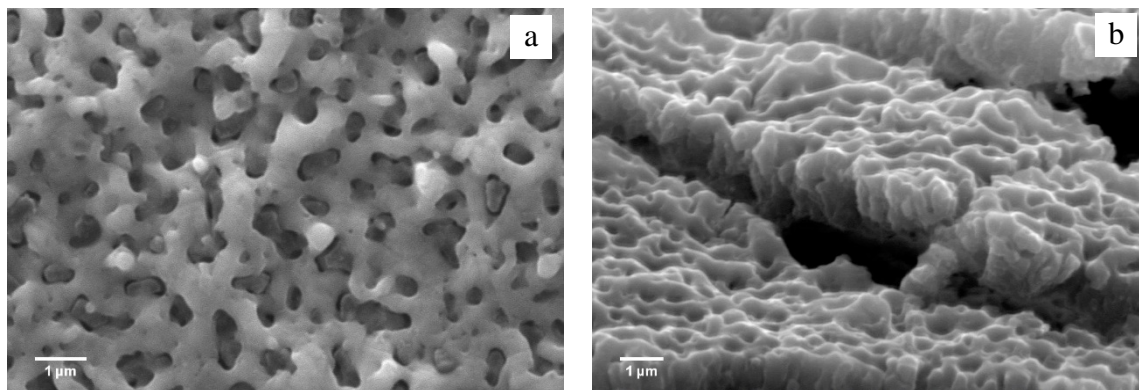


Figure 1. SEM micrographs of (a) the surface and (b) the cross-section of sample B-300.

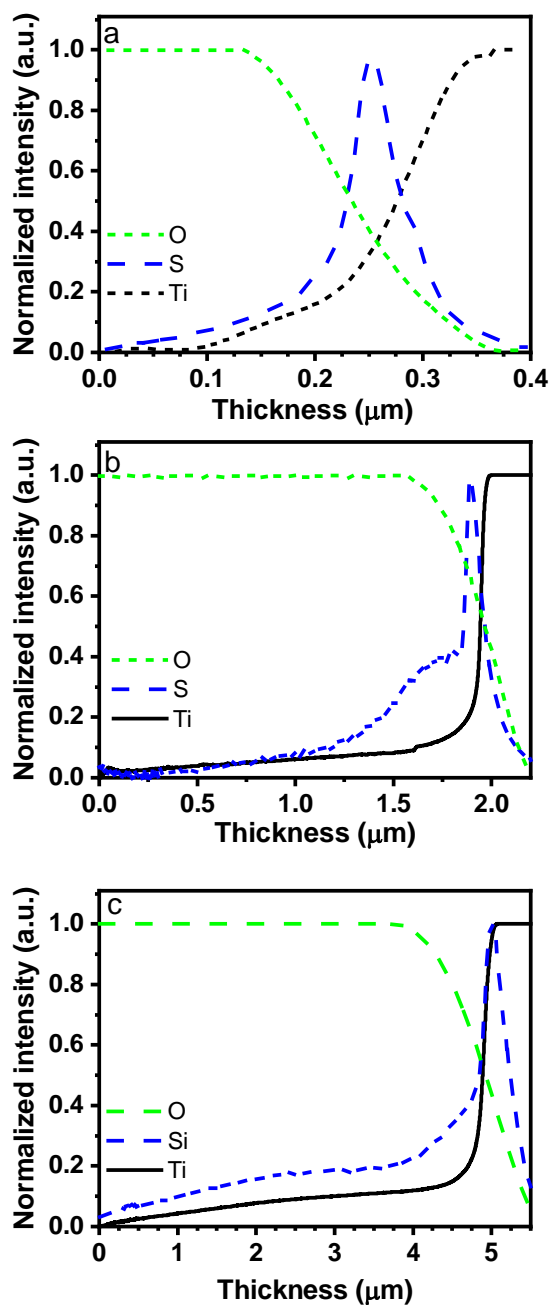


Figure 2. GD-OES in depth analysis for samples: (a) A-300, (b) B-90, and (c) C-90.

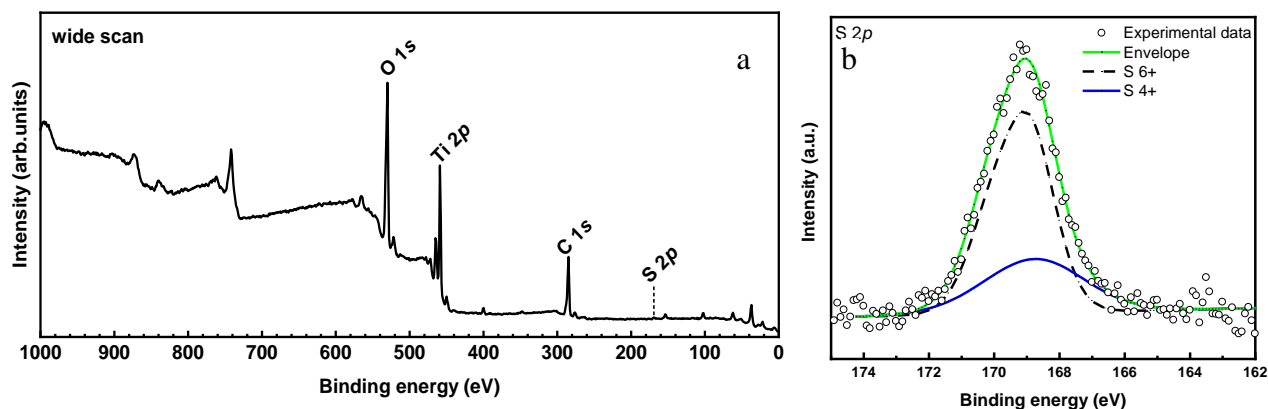


Figure 3. (a) XPS wide scan of sample C-5. The S peak is marked with a dashed line. (b) The S 2p signal at BE around 169.2 eV and its deconvolution.

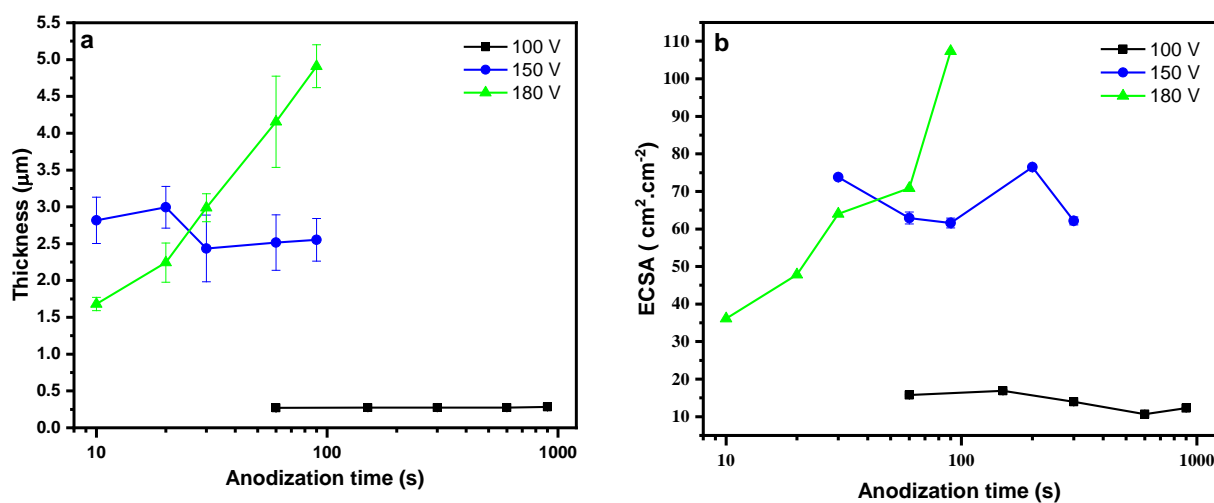


Figure 4. (a) Thickness and (b) ECSA of TiO₂ films obtained by PEO at different cell voltages and anodization times.

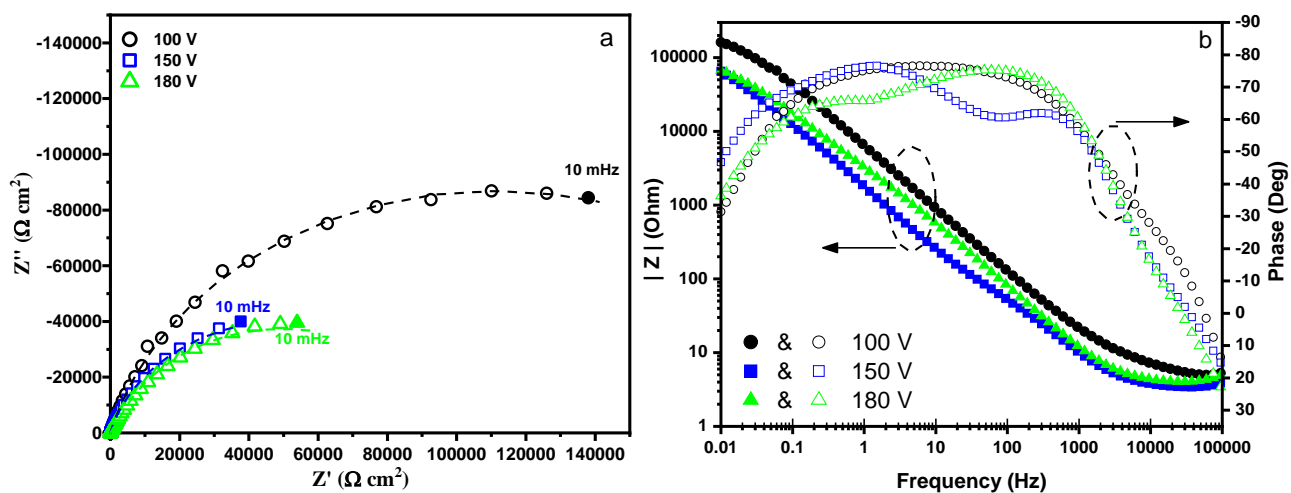


Figure 5. (a) Nyquist plots of experimental (symbols) and fitted (dashed lines) data for samples A-900, B-200 and C-90. The upper and lower insets are the corresponding electrical equivalent circuits, (b) Bode plots from the experimental data obtained with the same samples.

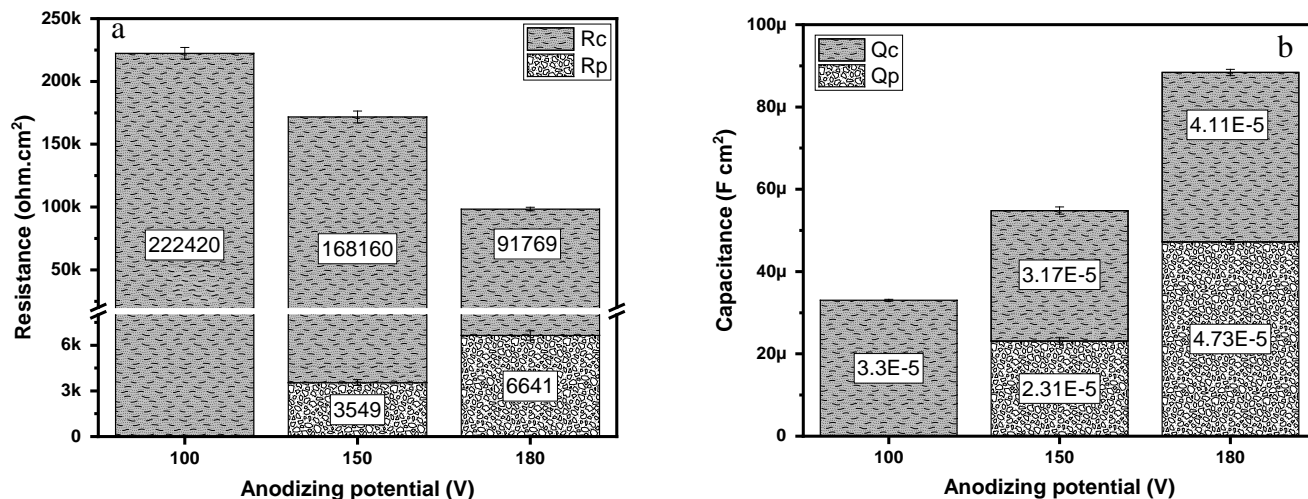


Figure 6. EIS data according to the proposed models: (a) resistance of the compact layer (R_c) and of the porous layer (R_p), (b) differential capacitance of the compact layer (Q_c) and of the porous layer (Q_p) for samples A-900, B-200 and C-90.

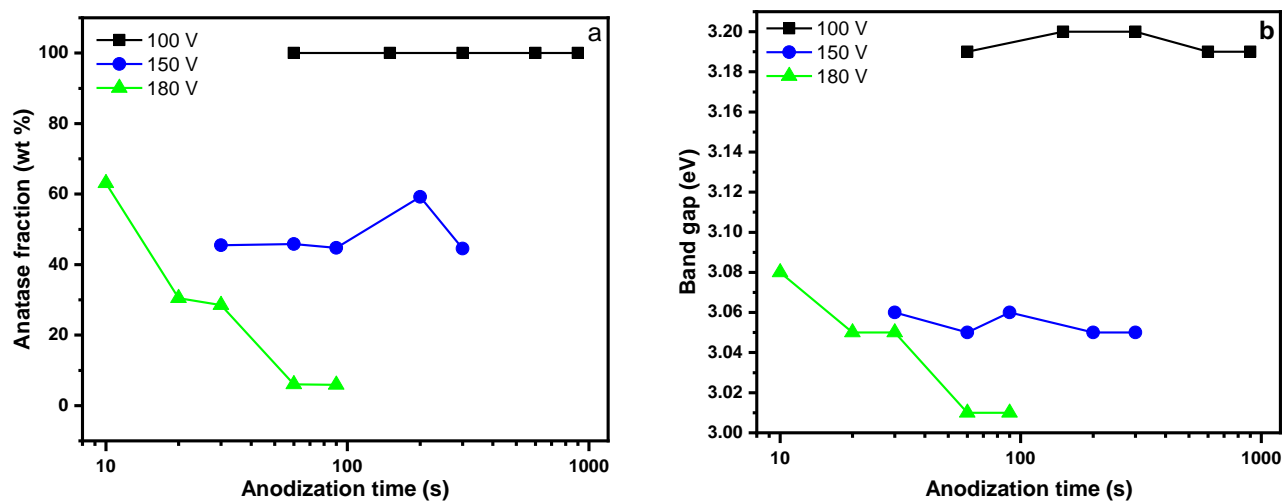


Figure 7. (a) Anatase fraction in the TiO_2 layer as a function of the anodization time at the three cell voltages. (b) Band-gap values of TiO_2 obtained at different cell voltages.

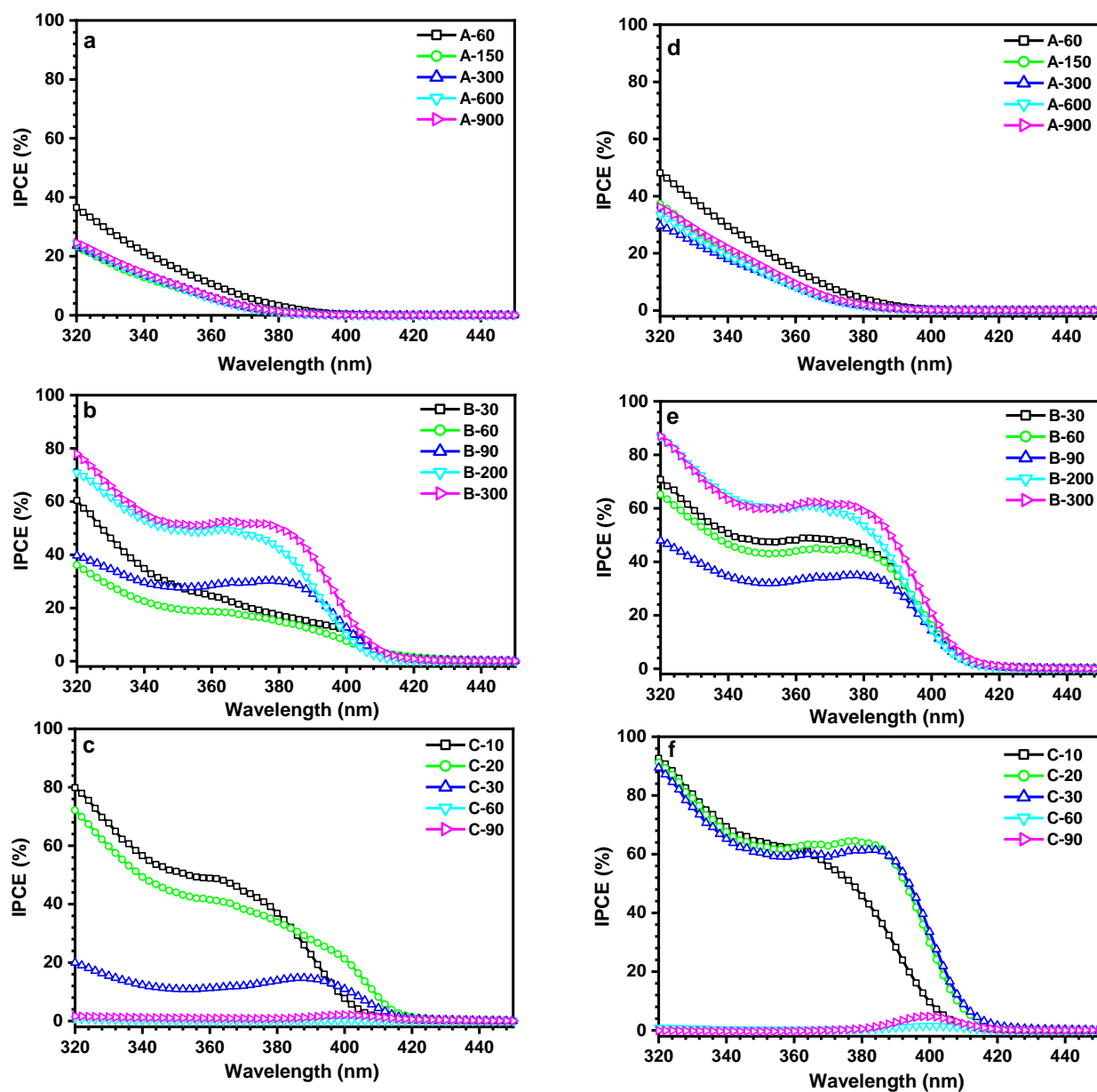


Figure 8. IPCE curves measured with TiO₂ electrodes obtained at (a,d) 100 V, (b,e) 150 V and (c,f) 180 V cell voltages with the anodization times indicated in the panels, (a,b,c) in the absence of applied bias and (e,f,g) under 0.6 V vs. SCE.

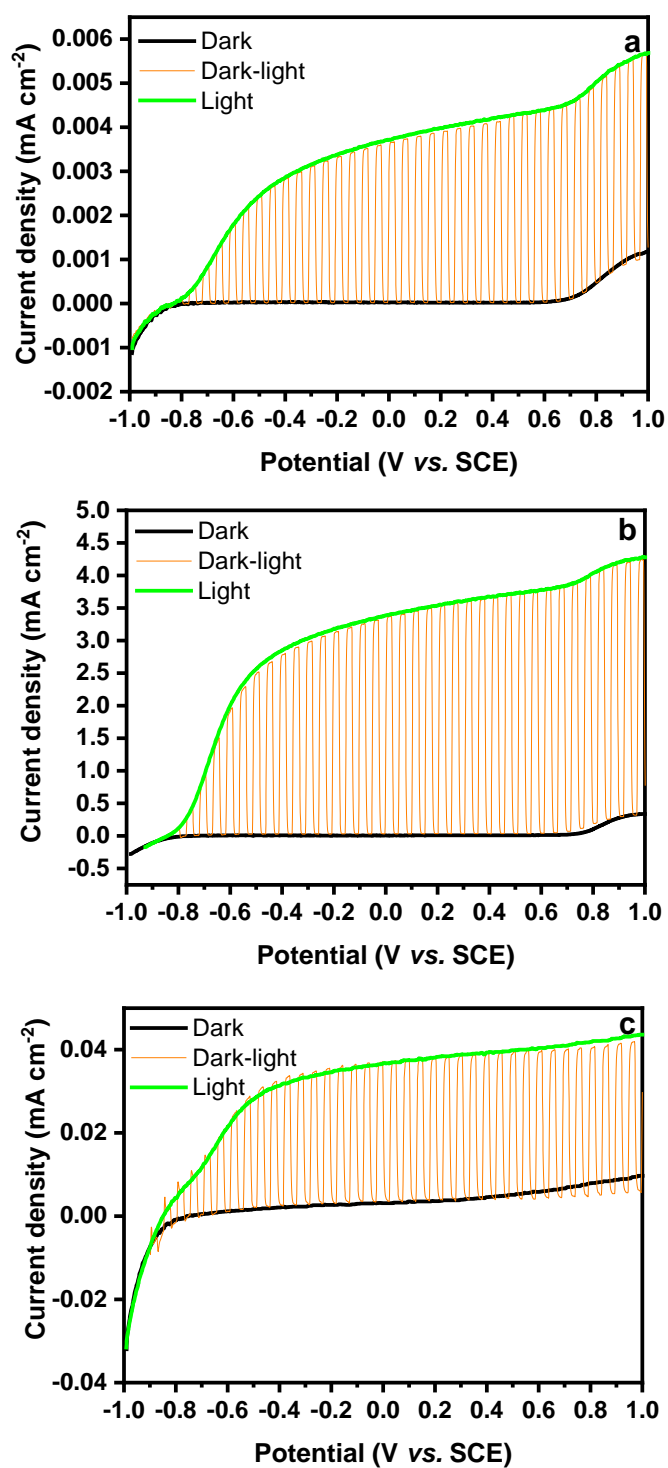


Figure 9. Linear sweep voltammetry curves recorded with selected electrodes: (a) A-60; (b) B-300, and (c) C-90, in 1.0 M NaOH with a scan rate of 5 mV s⁻¹. Photocurrent responses in the dark (black line), under chopped light (dark-light, orange line) and continuous irradiation (light, green line).

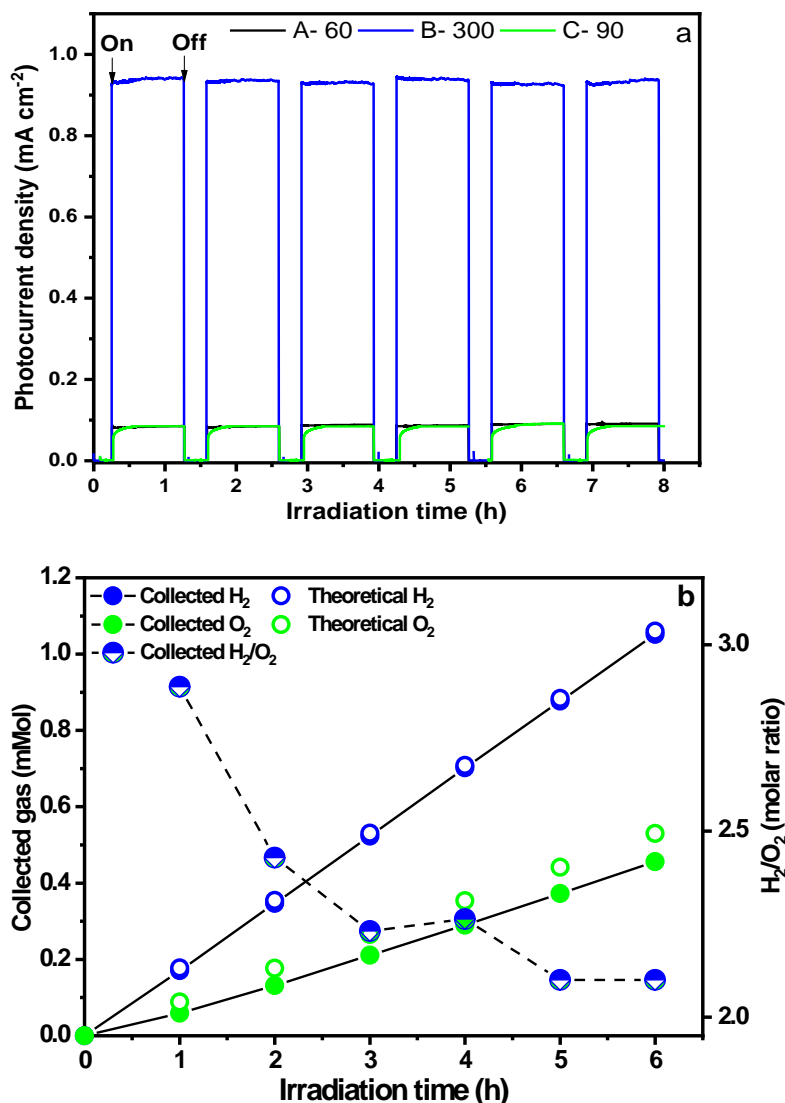


Figure 10. (a) Photocurrent density during H₂ and O₂ separate production under irradiation (AM 1.5 G, 100 mW.cm⁻²) for the three selected TiO₂ electrodes, (b) left ordinate: H₂ (blue) and O₂ (green) gases effectively collected under irradiation (full symbols) together with their theoretical values (empty symbols; right ordinate: experimental H₂/O₂ molar ratio (blue-green symbols).

Table 1. EIS fitting values: ohmic resistance (R_s), degree of non-ideal behavior of porous layer (n_p) and compact layer (n_c), Pearson's chi-square test (χ^2), effective capacitance of the porous layer ($C_{eff,p}$) and of the compact layer ($C_{eff,c}$), total effective capacitance (C_{eff}). CV total capacitance per geometric area unit (C_T/A).

Sample	R_s (Ω cm ²)	n_p	n_c	χ^2	$C_{eff,p}$ (μ F cm ²)	$C_{eff,c}$ (μ F cm ²)	C_{eff} (μ F cm ²)	C_T/A (μ F cm ²)
A-900	6.2	-	0.84	0.003	-	47.7	47.7	
B-200	3.9	0.74	0.72	0.001	9.9	60.8	70.7	65.8
C-90	3.9	0.87	0.8	0.001	39.7	57.3	97	92.3